2018 IEEE International Conference on Robotics and Automation (ICRA)
May 21-25, 2018, Brisbane, Australia

Design and Test of an *In-Vivo* Robotic Camera Integrated with Optimized Illumination System for Single-port Laparoscopic Surgery

Xiaolong Liu[1], Reza Yazdanpanah A.[1], Tao Zuo[3], Yong Guan[4], Gregory J. Mancini[2], Jindong Tan[1]

***Abstract*— This paper proposes a novel *in-vivo* robotic laparoscopic camera design with an optimized illumination system, which is a crucial component for achieving high imaging quality. The robotic camera design with three extendable wings can reserve sufficient on-board space to harbor the optimized illumination system without affecting the compactness of the camera. We contribute a freeform optical lens design method and develop three miniature optical lenses for the LEDs to achieve greater than 95% illumination uniformity, greater than 14,000 lx illuminance on a target plane with a distance of 100 mm, and greater than 89% optical efficiency. The prototype is implemented and experimentally tested, which demonstrates great performance of the *in-vivo* robotic laparoscopic camera and the significance of the optimized illumination system.**

I. Introduction

A laparoscopic camera is one of the most critical surgical instruments for minimally invasive surgery (MIS), which helps surgeons to extend their visual guidance into the abdominal cavity. From the past century to the present,"long-stick" laparoscopic cameras integrated with fiber-optic illumination system have been clinically adopted [1]. However, the form of the state-of-the-art commercialized laparoscopic cameras suffers poor triangulation capability, limited field of view, collision with other surgical instruments, and unintuitive manipulation, etc. [2]

To address the issues of the conventional "long-stick" laparoscopic cameras, research efforts have been made for developing *in-vivo* laparoscopic cameras. Researches have focused on the development of magnetic or on-board motor assisted manipulation/control mechanisms [3], [4], [5], [6], the camera lens cleaning [7], wireless transmission of imaging and control signals [8], camera-tissue interaction modeling, [9], and design/integration of camera systems [10], [11], [12], [13] for *in-vivo* robotic laparoscopic cameras. Although the developments of *in-vivo* laparoscopic cameras have achieved many progresses, the current designs are premature to be clinically adopted because of their inferior imaging qualities compared with commercial products.

One major issue of employing high definition (HD) or ultra HD on-board imaging sensors on an *in-vivo* robotic camera, is the challenge of designing an optimized illumination system integrated in *in-vivo* robotic cameras. For the same sensor size, the higher resolution results in the smaller pixel size, which has lower light sensitivity [14]. Thus, the illumination system should provide sufficient light intensity on target surgical areas for HD imaging sensors. In addition, to avoid bright centers and dark margins on acquired images, the light intensity on target surgical areas should be uniformly distributed. To maximally utilize light energy from on-board light sources, a well-designed illumination system should be capable of redirecting all the light rays within a camera's field of view (FOV). To the best of the authors' knowledge, there is no research on developing an illumination system to meet the above requirements for an *in-vivo* robotic laparoscopic camera. The scope of this paper is to propose a solution to overcome the two design challenges of the *in-vivo* illumination system: 1) the limited on-board space which makes it difficult to contain well-designed secondary optics for the LEDs; and 2) the non-imaging optical design methodology for the LEDs to control light beams according to the illumination requirements.

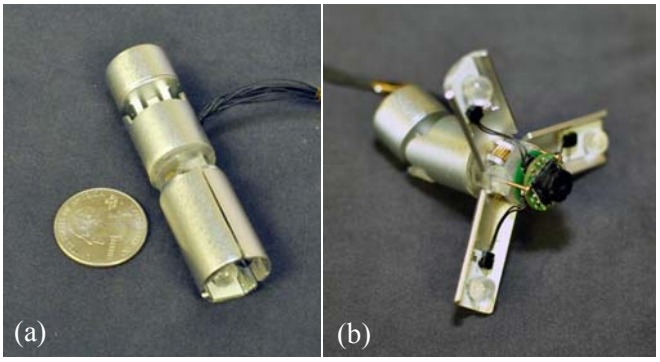

Fig. 1. Prototype of the *in-vivo* robotic laparoscopic camera. (a) shows the folded mode of the camera, which is used for inserting into a trocar; (b) shows the working mode of the camera.

In this paper, we propose an *in-vivo* robotic laparoscopic camera design, as illustrated in Fig. 1, which is capable of reserving sufficient on-board space for our optimized illumination system without affecting the compactness of the camera. The illumination system that harbored on the three wings consists of three high-efficiency white LEDs as the light sources and three miniature freeform optical lenses for controlling light rays. As the core task of designing the illumination system, the design of freeform lenses for extended light sources (LEDs) is a challenging task. This optical design problem is governed by a non-standard Monge-

[1]Xiaolong Liu (corresponding author), Reza Yazdanpanah Abdolmalaki and Jindong Tan are with Department of Mechanical, Aerospace and Biomedical Engineering, University of Tennessee, Knoxville, TN 37996, USA {xliu57,ryazdanp}@vols.utk.edu,tan@utk.edu

[2]Gregory J. Mancini is with Department of Surgery, University of Tennessee, Knoxville, TN 37996, USA GMancini@mc.utmck.edu

[3]Tao Zuo is with College of Information Science and Engineering, Wuhan University of Science and Technology, China zuotao@wust.edu.cn

[4]Yong Guan is with the College of Information Engineering, Capital Normal University, Beijing 100048, China guanyong@cnu.edu.cn

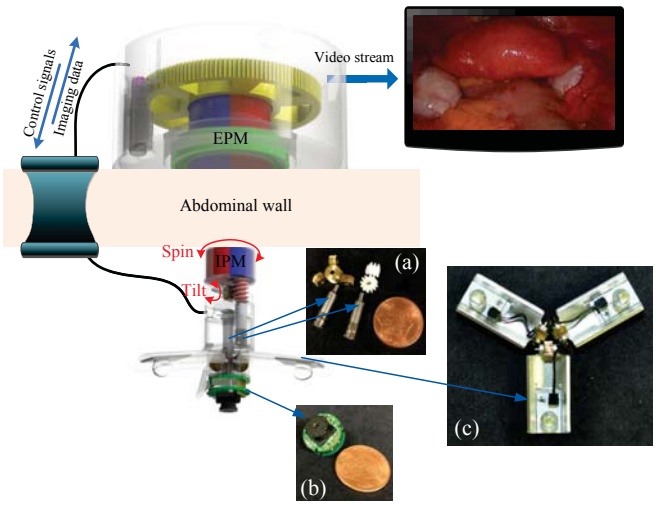

Fig. 2. Design details of the *in-vivo* robotic camera system. (a) the on-board actuators and worm-gear sets; (b) the imaging system; (c) the illumination system.

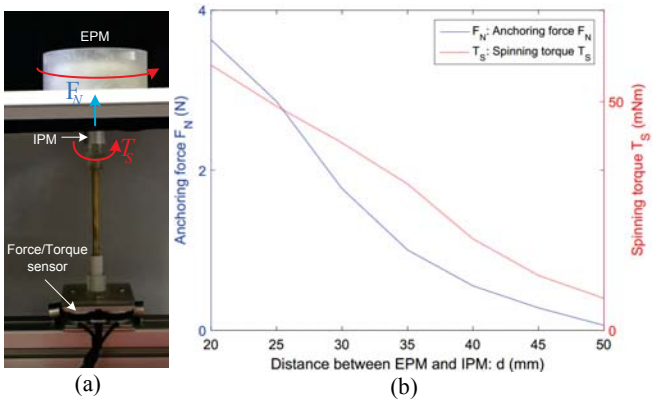

Fig. 3. Anchoring force and Spinning torque experimental tests. (a) Magnetic force and torque measurement system setup. The IPM and the EPM are both sealed in cases. (b) Measurement data of the anchoring force and the spinning torque.

Ampere equation, which is a highly nonlinear second-order partial differential equation (PDE) [15], [16]. In this paper, we contribute a new ray-mapping based numerical method to design the freeform lenses for our illumination system. The proposed method features easy numerical implementation and fast convergent speed. A complete prototype of the *in-vivo* camera with optimized illumination system is implemented and tested. The experiments demonstrate great performance of the *in-vivo* robotic laparoscopic camera and the significance of the optimized illumination system.

II. Design of *in-vivo* Robotic Camera

The *in-vivo* robotic laparoscopic camera with an outer diameter of 18 mm can be inserted in a SILS port (e.g. Covidien port, Medtronic Inc.). The total length of the camera is 72 mm when the wings are folded, and 45 mm when the wings are extended. The external magnetic anchoring/driving unit shown in Fig. 2 generates a magnetic coupling with the on-board permanent magnet, and fixes the robotic camera against the inner side of the abdominal wall. The soft cable connected with the external anchoring/driving unit is used for control signals communication, on-board power supply, imaging data acquisition, prevention of unexpected robot falling down, and the robotic camera retrieval after surgeries.

A. External Magnetic Anchoring/Driving Unit

The external magnetic anchoring/driving unit, which has a diameter of 80 mm and a height of 50 mm, includes (1) a diametrically magnetized permanent magnet for magnetic coupling with the internal permanent magnet (IPM); (2) a miniature DC motor plus a set of driving gears for controlling the rotational motion of the magnet; and (3) a controller board to send control signals or retrieve imaging data, as illustrated in Fig. 2. The magnetic attractive force between the external permanent magnet (EPM) and the IPM provides the anchoring force for the robotic camera. Due to the magnetic coupling, a rotational motion of the EPM will generate a spinning motion of the IPM, and consequently the whole camera. And the repositioning of the external unit will drag the camera to a new location inside the abdominal cavity.

Fig. 3(a) shows the experimental setup for testing the magnetic anchoring force, spinning torque generated from the interaction between the EPM and the IPM. A six-axis force/torque sensor (HEX-58-RF-2000N, Optoforce Inc.) was employed to measure the experimental data. The IPM was rigidly fixed with the force/torque sensor along Z axis. The normal range of an abdominal wall thickness is 30 mm~50 mm [17]. In this evaluation, we set the distance between the IPM and the EPM from 20 mm to 50 mm with 5 mm sampling interval.

Fig. 3(b) shows the experimental measurements of the anchoring force and spinning torque. The total weight of the robotic camera is 43.8 g. The anchoring force F_N represents the magnetic attractive force minus the camera weight. F_N is 4.06 N when d=20 mm, and 0.492 N when d=50 mm. The maximum pressure applied on the inner abdominal wall 2.31 psi is less than the safe threshold 3.45 psi for preventing undesired histological damage [18]. The smallest spinning torque T_S in Fig. 3(b) applied on the IPM is 7 mNm when d=50 mm. The frictional torque that resists the spinning motion is calculated as 3.3 mNm at d=20 mm, and 0.1 mNm at d=50 mm. Thus, the torque T_S is sufficient to generate a spinning motion of the camera.

B. On-board Actuation Mechanism

In addition to the spinning motion, the robotic camera has an actuation mechanism to generate tilt motion for adjusting the camera's visual directions. And another actuation mechanism is designed to control the opening angles of the wings that carry the illumination system. Fig. 2(a) demonstrates the mechanical structures of the actuation mechanisms. The actuators are stepper motors with diameters of 4 mm, lengths of 14.42 mm, and 125:1 planetary gearheads (ZWBMD004004-125, Shenzhen Zhaowei Machinery & Electronics Inc.). The stepper motor can deliver a torque of 10 mNm at continuous

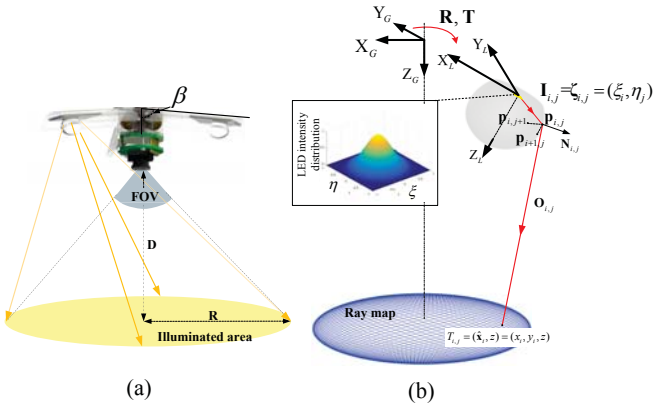

Fig. 4. (a) Conceptual demonstration of illumination system setup. (b) Ray-mapping based freeform optical lens design for the LEDs.

operation. The customized worm gear sets for the tilt actuator and the wings' actuator have reduction ratios of 12:1 and 20:1 respectively. Our design provide a tilt motion range of 49°, which is capable of visually covering all the areas inside the abdominal cavity.

C. Imaging System

Fig. 2(b) shows the configuration of imaging system, which employs (1) an OmniVision OV7955 CMOS sensor with an imaging array size of 672×492, an optical size of $1/3.7''$, a sensitivity of 16 V/lux-sec, a pixel size of $6\,\mu m \times 6\,\mu m$, a capture rate of 60 fps, and NTSC analog output; (2) a $1/4''$ lens (DSL756, Sunex, Inc.) with a focal length of 3.8 mm, a diagonal field of view 60°, and multi-megapixel resolution; and (3) a compatible lens holder (CMT756, Sunex, Inc.) for the DSL756 lens.

III. Design of Optimized Illumination System

An optimized illumination system should deliver sufficient luminous flux and high illuminance uniformity with high optical efficiency that reduces the number of LEDs. To determine required illumininace of the illumination system, we refer to [3] that adopts a comparable sensor as ours. A maximum illuminance of 4,000 lx at a distance of 50 mm was reported. Considering 50 mm ~ 100 mm working distance between the camera and a target surgical area, we conservatively require our illumination system to uniformly deliver a maximum illuminance of 10,000 lx at a distance of 100 mm.

A. Requirements of Optimized Illumination

High optical efficiency means that the light sources should only illuminate the areas within the camera's FOV, as shown in Fig. 4(a). Recall the 60° diagonal FOV of the imaging system. When D is set as 100 mm, the minimal illuminated area should be with a radius of $R_{FOV} = 57.7$ mm. In our design, we set the radius of illumination area $R = 80$ mm when $D = 100$ mm. To achieve the illuminance of 10,000 lx in this area, the total luminous flux from the light sources should be at least 201 lm.

In this prototype, we employ three Cree Xlamp XQ-E white LEDs with the color temperature of 5700 K and the total luminous flux of 354 lm at 350 mA (118 lm from each LED). The LEDs are soldered on aluminum PCBs for better heat dissipation, and fixed on the wings. To achieve the illumination requirements discussed above, we employ the freeform optical lens design algorithm that designed in our prior work [19].

B. Freeform Optical Lens Design for LEDs

The freeform optics design problem is usually governed by a non-standard Monge-Ampere equation [15], [16], which is second-order highly nonlinear PDE. Because of the highly nonlinearity of this problem, it is quite challenging to find an easy-to-implement and effective numerical method to obtain a converged solution. Instead of solving the non-standard Monge-Ampere equation directly, we proposed a ray-mapping based freeform lens design method, which enforces integration conditions to guarantee a smooth continuous optical surface.

According to the law of conservation of energy, a ray map $\hat{\boldsymbol{x}} = \phi(\boldsymbol{\zeta})$ defines the relationship between light ray directions $\boldsymbol{\zeta} = (\xi, \eta)$ and incident points $\hat{\boldsymbol{x}} = (x, y)$ on a target area, as illustrated in Fig. 4(b). By representing the ray mapping solution as the gradient of a convex potential $\phi = \nabla u$, we can formulate the ray-mapping problem in

$$\det \nabla^2 u(\boldsymbol{\zeta}) = \frac{E_s(\boldsymbol{\zeta})}{E_t(\nabla u(\boldsymbol{\zeta}))}, \tag{1}$$

which is a standard Monge-Ampere equation. Numerical solvers that employed for ray map computation are tricky to numerically implement [20], [21]. Inspired by the fact that a weak solution of a lower order nonlinear PDE can be approximated by a sequence of higher order quasi-linear PDEs [22], [23], we introduce an effective numerical method to compute the solution of Eq. (1) for the freeform optical lens design.

C. Ray Map Computation

We employ a sequence of fourth-order quasi-linear PDEs, i.e. the biharmonic operator, to approximate the numerical solution of the second-order nonlinear PDE in Eq. (1). The approximated solution u^ϵ can be computed from the following quasi-linear PDE and a Newmann boundary condition (BC):

$$-\epsilon \Delta^2 u^\epsilon + \det \nabla^2 u^\epsilon(\boldsymbol{\zeta}) - \frac{E_s(\boldsymbol{\zeta})}{E_t(\nabla u^\epsilon(\boldsymbol{\zeta}))} = 0, \quad \boldsymbol{\zeta} \in \Omega_s \tag{2}$$

$$\text{BC}: \quad f(\nabla u^\epsilon(\boldsymbol{\zeta})) = 0, \quad \boldsymbol{\zeta} \in \partial\Omega_s \tag{3}$$

where $\epsilon > 0$ and $\lim_{\epsilon \to 0^+} u^\epsilon$ is the weak solution of Eq. (2) if the limit exists. The computation strategy is to firstly set a sequence of gradually reduced constant values for ϵ, e.g. $10^{-1}, 10^{-2}$, and so on. In each iteration, the value of ϵ is updated according to the preset value sequence, and the solution of u^ϵ at the current iteration is initialized by the solution from the previous iteration.

By discretizing Eq. (2) and (3), a system of nonlinear equations can be formulated as

$$\boldsymbol{F}(\boldsymbol{U}^\epsilon) = 0, \tag{4}$$

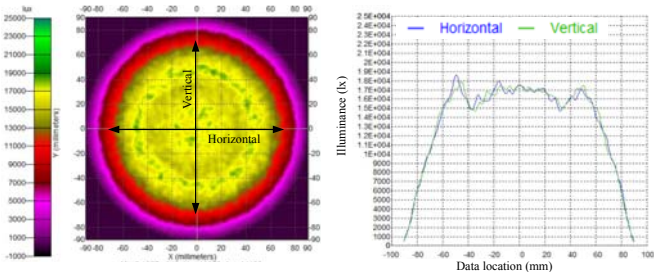

Fig. 5. The simulation results of the illuminance distribution on target plane by lighting three LEDs at 350 mA when D=100 mm.

where $\boldsymbol{U}^{\epsilon}$ is a vector that contains the discretized values of u^{ϵ} in Ω_s. The Newton's method is employed as the numerical solver to compute Eq. (4).

D. Optical Surface Construction

According to the computed ray map, each light ray from the source $\mathbf{I}_{i,j}$, which is represented in the coordinate system $\Sigma_L\{X_L, Y_L, Z_L\}$, is mapped to a point on the target plane $\mathbf{T}_{i,j}$ represented in $\Sigma_G\{X_G, Y_G, Z_G\}$, as shown in Fig. 4(b). The rotational matrix $\mathbf{R}$ and translational vector $\mathbf{T}$ characterize the relationship between Σ_G and Σ_L. We employ an easy-to-implement method proposed in [24] to construct an initial optical surface. However, due to the accumulated errors, this method can not guarantee the computed normal vectors $\mathbf{N}_{i,j}$ at $\mathbf{p}_{i,j}$ are perpendicular to $\overrightarrow{\mathbf{p}_{i,j}\mathbf{p}_{i+1,j}}$ and $\overrightarrow{\mathbf{p}_{i,j}\mathbf{p}_{i,j+1}}$. We introduce an optimization technique to correct the normal vectors by adjusting the surface points. A surface point $\mathbf{p}_{i,j}$ and the normal vector $\mathbf{N}_{i,j}$ should comply the constraints:

$$(\boldsymbol{p}_{i+1,j} - \boldsymbol{p}_{i,j})\boldsymbol{N}_{i,j} = 0, \tag{5}$$

$$(\boldsymbol{p}_{i,j+1} - \boldsymbol{p}_{i,j})\boldsymbol{N}_{i,j} = 0. \tag{6}$$

Then for each surface point, an optimization function can be constructed

$$F_{i,j}(\boldsymbol{\rho}) = ||(\rho_{i+1,j}\boldsymbol{I}_{i+1,j} - \rho_{i,j}\boldsymbol{I}_{i,j}) \cdot \boldsymbol{N}_{i,j}|| + ||(\rho_{i,j+1}\boldsymbol{I}_{i,j+1} - \rho_{i,j}\boldsymbol{I}_{i,j}) \cdot \boldsymbol{N}_{i,j}|| = 0, \tag{7}$$

where $\rho_{i,j}$ represents the distance between the light source and the surface point. The nonlinear least-squares method is adopted to minimize $\sum_{i=1}^{N_i}\sum_{j=1}^{N_j} F_{i,j}(\boldsymbol{\rho})^2$. The optical surface can be represented by using the optimized surface points with NURBS [25] method.

E. Performance Evaluation of Freeform Optical Lens

We initially evaluate the performance of the freeform optical lens by using an optical design software (TracePro, Lambda Research Corp.). The simulation setup is illustrated in Fig. 4 with D = 100 mm. In the simulation, we employ 500, 000 rays emitted from each LED with a luminous flux of 118 lm. Fig. 5 shows the illuminance distribution by lighting up three LEDs. The uniformity of an illuminance distribution can be quantified by

$$\text{Uniformity} = \left(1 - \frac{\sigma}{\mu}\right) \times 100, \tag{8}$$

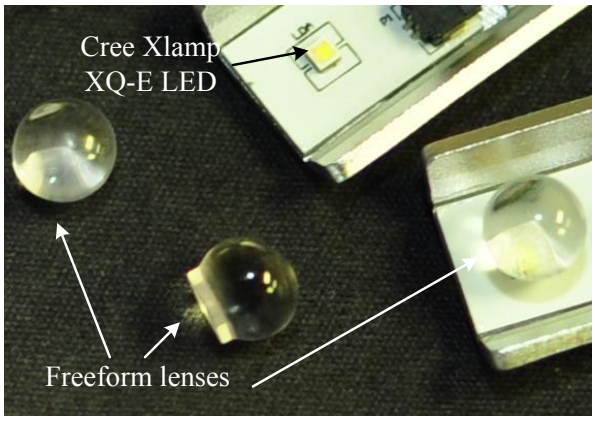

Fig. 6. Fabrication of the designed freeform optical lenses.

where σ is the standard deviation, and μ is the mean of collected illuminance data. The average illuminance of Fig. 5 is 16, 981 lx with considering Fresnel losses. The optical efficiency is 89.45%. The illuminance uniformities are 96.33% in horizontal and 96.79% in vertical.

IV. Experiments

In this section, we firstly introduce the manufacturing of the freeform optical lenses. Then, an experimental platform was setup for illumination tests. At last, we demonstrate the manipulation tests of the robotic camera.

A. Freeform optical lens manufacturing

The freeform lens designed in Section III was manufactured by an ultra-precision vertical machine (UVM-450C, Toshiba Inc.). The manufacturing accuracy is ±1 µm. The material of the lenses was selected as PMMA (Polymethyl Methacrylate) with a refractive index of 1.49 and visible light transmittance of 92%. Fig. 6 shows the fabricated freeform optical lenses, Cree Xlamp XQ-E white LEDs, and LED circuit boards attached on the wings.

B. Illuminance uniformity test

Fig. 7(a) and (b) show the experimental setups for testing the illuminance uniformity on the target plane. In Fig. 7(a), the robotic camera was fixed on a moving track, which is used for adjusting the distance D between the camera and the target plane. We employ an acrylic panel with 55% transparency as the illumination plane. A DSLR camera was utilized to record illuminance distributions on the acrylic plane. To measure the illumiance at a specific distance D, a lux meter (Extech LT-40, FLIR Systems Inc.) was positioned at the central axis of the camera.

Fig. 7(b) demonstrates the illuminance distribution on the acrylic panel with D=100 mm. The illuminated area is with a radius of R=77 mm, which is capable of covering the camera's 60° FOV. The LEDs were driven by 350 mA current inputs with the color temperature at 5700 K. The total output luminous flux was 354 lm. The illuminance uniformities in Fig. 7(b) were computed with the image intensity data. The illuminance uniformities are 95.47% in horizontal and

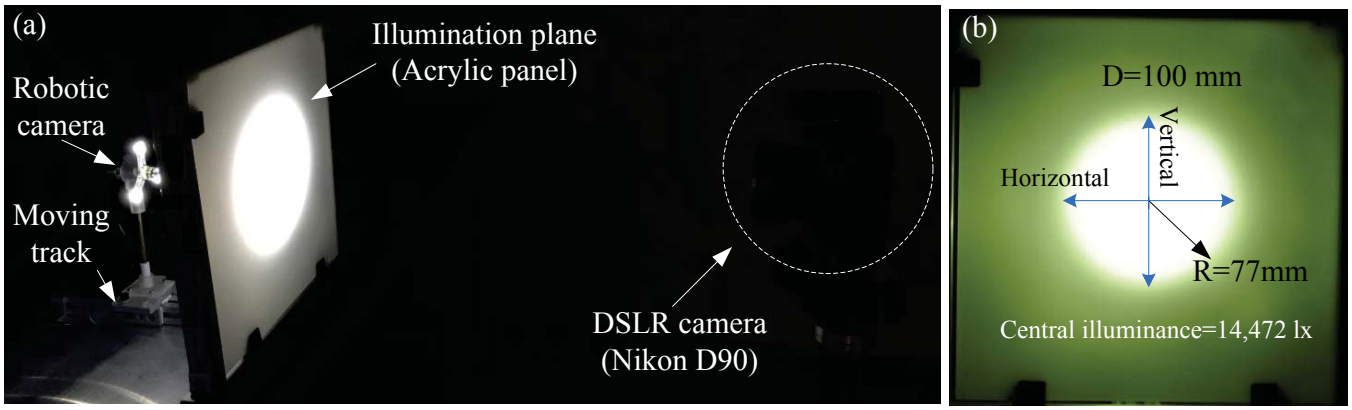

Fig. 7. Experimental tests of the optimized illumination system. (a) shows the experiment setups for testing the illuminance uniformities; (b) shows the recorded illuminance distribution on the acrylic plane with the camera-to-plane distances D=100 mm.

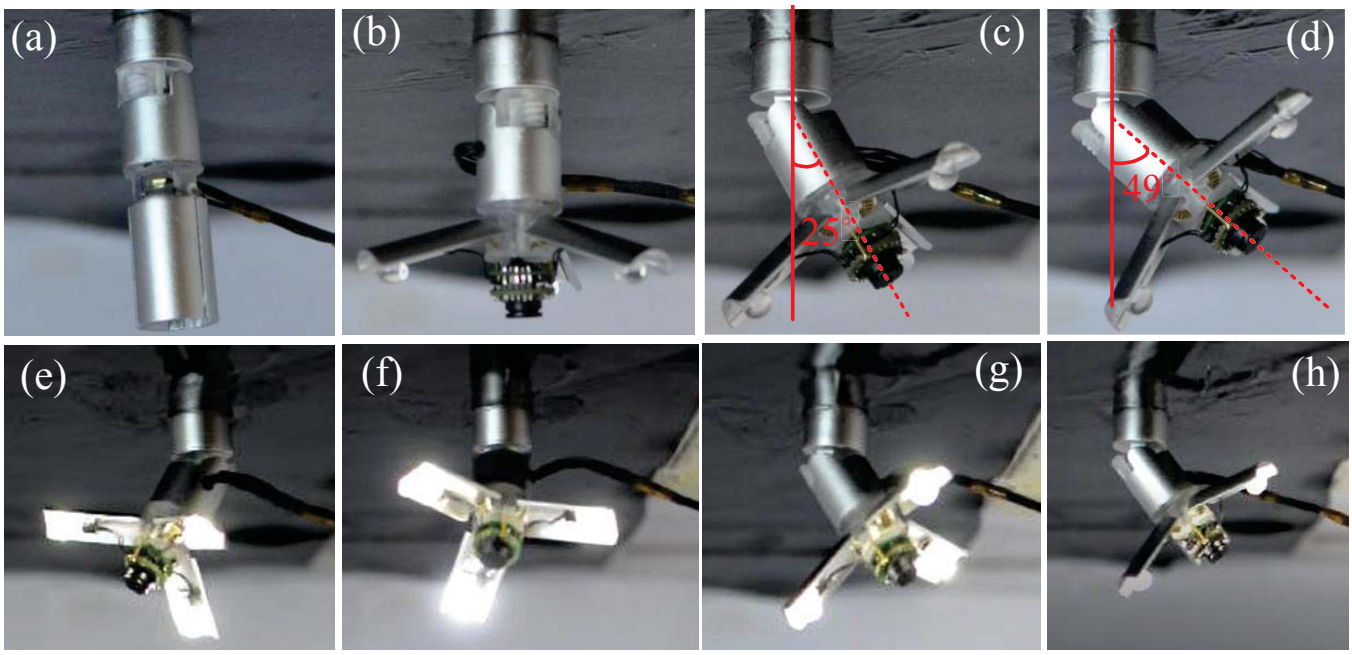

Fig. 8. Manipulation tests of the robotic camera in a simulated abdominal cavity. (a) shows an initial pose after inserting the camera inside the simulated abdominal cavity; (b) shows the working mode of the robotic camera by opening the wings; (c) and (d) show the tilt motion tests of the camera; (e)-(f) show the spinning motion tests of the camera.

95.22% in vertical. The central illuminance in Fig. 7(b) was measured as 14, 472 lx. The experimental results indicate that our illumination system design satisfies all the requirements proposed in Section III-A.

C. Robotic camera manipulation tests

Fig. 8 shows the manipulation test of the robotic camera. Fig. 8(a) demonstrates the initial pose of the robotic camera after being inserted in the simulated abdominal cavity. Then the wings are extended to expose the camera and the illumination system, as shown in Fig. 8(b). Fig. 8(c) and (d) show the tilt motion tests with 25° and 49° tilt angles. Fig. 8(e)-(h) show the spinning motion of the robotic camera to visually cover all the areas inside the abdominal cavity.

V. Conclusion

In this paper, we present an *in-vivo* robotic camera with an optimized illumination system for single-port laparoscopic surgery. To improve the imaging quality for *in-vivo* laparoscopic cameras, we contribute an innovative transformable robot, which is able to carry well-designed freeform optical lenses for increasing illuminance, and improving illumination uniformity and optical efficiency on target surgical areas. For designing the freeform optical lenses, we contribute an effective ray-mapping based freeform optical lens design method, which is able to achieve greater than 95% illuminance uniformity and greater than 89% optical efficiency. The experimentally evaluations validate the design performance of the optimized illumination system.

The achieved optimized illumination system is the first

step of our project. At the time of the acceptance date of this paper, we are working on extending this design with an ultra HD imaging sensor and optimized imaging optical lens to achieve superior imaging quality for the *in-vivo* robotic laparoscopic camera.

REFERENCES

[1] S. Spaner and G. Warnock, "A brief history of endoscopy, laparoscopy, and laparoscopic surgery," *J Laparoendosc Adv Surg Tech A*, vol. 7, no. 6, pp. 369–373, 1997.

[2] P. P. Rao, P. P. Rao, and S. B. S, "Single-incision laparoscopic surgery - current status and controversies," *Journal of Minimal Access Surgery*, vol. 7, no. 1, pp. 6–16, 2011.

[3] M. Simi, M. Silvestri, C. Cavallotti, M. Vatteroni, P. Valdastri, A. Menciassi, and P. Dario, "Magnetically activated stereoscopic vision system for laparoendoscopic single-site surgery," *IEEE/ASME Trans. Mechatronics*, vol. 18, no. 3, pp. 1140–1151, 2013.

[4] X. Liu, G. J. Mancini, and J. Tan, "Design of a unified active locomotion mechanism for a capsule-shaped laparoscopic camera system," in *Robotics and Automation (ICRA), 2014 IEEE International Conference on*, pp. 2449–2456, 2014.

[5] X. Liu, G. J. Mancini, Y. Guan, and J. Tan, "Design of a magnetic actuated fully insertable robotic camera system for single-incision laparoscopic surgery," *IEEE/ASME Trans. Mechatronics*, vol. 21, no. 4, pp. 1966–1976, 2016.

[6] X. Liu, A. R. Yazdanpanah, G. J. Mancini, and J. Tan, "Control of a magnetic actuated robotic surgical camera system for single incision laparoscopic surgery," in *2015 IEEE International Conference on Robotics and Biomimetics (ROBIO)*, pp. 1396–1402, Dec 2015.

[7] A. R. Yazdanpanah, X. Liu, N. Li, and J. Tan, "A novel laparoscopic camera robot with in-vivo lens cleaning and debris prevention modules," in *2017 IEEE/RSJ International Conference on Intelligent Robots and Systems (IROS)*, pp. 3669–3674, Sept 2017.

[8] C. A. Castro, A. Alqassis, S. Smith, T. Ketterl, Y. Sun, S. Ross, A. Rosemurgy, P. P. Savage, and R. D. Gitlin, "A wireless robot for networked laparoscopy," *IEEE Trans. Biomed. Eng.*, vol. 60, no. 4, pp. 930–936, 2013.

[9] A. R. Yazdanpanah, X. Liu, and J. Tan, "Modeling and analysis of a laparoscopic camera's interaction with abdomen tissue," in *2017 IEEE International Conference on Robotics and Automation (ICRA)*, pp. 4227–4232, May 2017.

[10] T. Hu, P. K. Allen, N. J. Hogle, and D. L. Fowler, "Insertable surgical imaging device with pan, tilt, zoom, and lighting," *Int. J. Robot. Res.*, vol. 28, no. 10, pp. 1373–1386, 2009.

[11] B. S. Terry, A. D. Ruppert, K. R. Steinhaus, J. A. Schoen, and M. E. Rentschler, "An integrated port camera and display system for laparoscopy," *IEEE Trans. Biomed. Eng.*, vol. 57, no. 5, pp. 1191–1197, 2010.

[12] J. Cadeddu, R. Fernandez, M. Desai, R. Bergs, C. Tracy, S. Tang, P. Rao, M. Desai, and D. Scott, "Novel magnetically guided intra-abdominal camera to facilitate laparoendoscopic single-site surgery: initial human experience.," *Surg. Endosc.*, vol. 23, no. 8, pp. 1894–1899, 2009.

[13] P. Swain, R. Austin, K. Bally, and R. Trusty, "Development and testing of a tethered, independent camera for notes and single-site laparoscopic procedures.," *Surg. Endosc.*, vol. 24, no. 8, pp. 2013–21, 2010.

[14] J. Farrell, F. Xiao, and S. Kavusi, "Resolution and light sensitivity tradeoff with pixel size," in *In Proceedings of the SPIE Electronic Imaging 06 Conference*, vol. 6069, pp. 211–218, 2006.

[15] J. S. Schruben, "Formulation of a reflector-design problem for a lighting fixture," *J. Opt. Soc. Am.*, vol. 62, no. 12, pp. 1498–1501, 1972.

[16] H. Ries and J. Muschaweck, "Tailored freeform optical surfaces," *J. Opt. Soc. Am. A*, vol. 19, no. 3, pp. 590–595, 2002.

[17] C. Song, A. Alijani, T. Frank, G. Hanna, and A. Cuschieri, "Mechanical properties of the human abdominal wall measured in vivo during insufflation for laparoscopic surgery," *Surgical Endoscopy And Other Interventional Techniques*, vol. 20, no. 6, pp. 987–990, 2006.

[18] S. Best, W. Kabbani, D. Scott, R. Bergs, H. Beardsley, R. Fernandez, L. Mashaud, and J. Cadeddu, "Magnetic anchoring and guidance system instrumentation for laparo-endoscopic single-site surgery/natural orifice transluminal endoscopic surgery: lack of histologic damage after prolonged magnetic coupling across the abdominal wall.," *Urology*, vol. 77, no. 1, pp. 243–7, 2011.

[19] X. Liu, R. Y. Abdolmalaki, G. J. Mancini, and J. Tan, "Optical design of an in vivo laparoscopic lighting system," *Journal of Biomedical Optics*, vol. 22, pp. 22 – 22 – 15, 2017.

[20] B. D. Froese, "A numerical method for the elliptic Monge-Ampère equation with transport boundary conditions," *SIAM J. Sci. Comput.*, vol. 34, no. 3, pp. A1432–A1459, 2012.

[21] M. M. Sulman, J. Williams, and R. D. Russell, "An efficient approach for the numerical solution of the Monge-Ampère equation," *Appl. Num. Math.*, vol. 61, no. 3, pp. 298 – 307, 2011.

[22] M. G. Crandall and P. L. Lions, "Viscosity solutions of hamilton-jacobi equations," *Trans. Amer. Math. Soc.*, vol. 277, no. 1, pp. 1–42, 1983.

[23] X. Feng and M. Neilan, "Vanishing moment method and moment solutions for fully nonlinear second order partial differential equations," *J. Sci. Comput.*, vol. 38, no. 1, pp. 74–98, 2009.

[24] L. Wang, K. Qian, and Y. Luo, "Discontinuous free-form lens design for prescribed irradiance," *Appl. Opt.*, vol. 46, no. 18, pp. 3716–3723, 2007.

[25] L. Piegl and W. Tiller, *The NURBS Book (2Nd Ed.)*. New York: Springer Science & Business Media, 1997.